Dynamics of laminar circular jet impingement upon convex cylinders

T. H. New and J. Long

Citation: Physics of Fluids (1994-present) **27**, 024109 (2015); doi: 10.1063/1.4913498
View online: http://dx.doi.org/10.1063/1.4913498
View Table of Contents: http://scitation.aip.org/content/aip/journal/pof2/27/2?ver=pdfcov
Published by the AIP Publishing

PHYSICS OF FLUIDS **27**, 024109 (2015)

Dynamics of laminar circular jet impingement upon convex cylinders

T. H. New[a] and J. Long
School of Mechanical and Aerospace Engineering, Nanyang Technological University, 50 Nanyang Avenue, Singapore 639798, Singapore

(Received 10 June 2014; accepted 11 February 2015; published online 26 February 2015)

Flow dynamics associated with a laminar circular jet impinging upon a convex cylinder has been investigated by laser-induced fluorescence and digital particle-image velocimetry techniques. Cylinder-to-jet diameter ratios of 1, 2, and 4 were investigated, while the jet-to-cylinder separation distance was kept at four jet diameters throughout. Flow visualization and λ_2 criterion results show that once the jet ring-vortices impinge upon the cylindrical surface, they move away from the impingement point by wrapping themselves partially around the surface. As the cylinder diameter increases, wall boundary layer separation, vortex dipole formation, and separation locations are initiated earlier along the cylindrical surface, producing significantly larger wakes. Along the cylinder straight-edges, ring-vortex cores are significantly smaller after impingement. This is due to accentuated vortex-stretching caused by partial wrapping around the cylindrical surface by the ring-vortices, on top of their movement away from the impingement point. Interestingly, vortex dipoles demonstrate a strong tendency to travel upstream and interact with other upstream vortex dipoles, instead of moving downstream gradually seen for flat-surface jet-impingements. Wall shear stress results are also presented to quantify the effects of cylinder diameter-ratio on surface skin friction distribution. Finally, these preceding observations are corroborated and explained in a three-dimensional flow dynamics model presented here. © *2015 AIP Publishing LLC.* [http://dx.doi.org/10.1063/1.4913498]

I. INTRODUCTION

Jet impingements have long been used as one of the most direct and efficient ways to remove heat from or impart heat to solid surfaces. This can be readily observed in their applications in paper, textile, glass and metal sheet manufacturing, cooling of electronic components, as well as aircraft de-icing and cooling of gas turbine blades, just to name a few. It should not come as a surprise then, that there had been significant number of investigations devoted towards isolating the relationships between the impinging jet configurations to their flow dynamics and heat transfer efficacies. In particular, earlier studies on the flow structures and behaviour resulting from jet impingement of flat-surfaces include Donaldson and Snedeker,[1] Didden and Ho,[2] Landreth and Adrian,[3] Popiel and Trass,[4] Fairweather and Hargrave,[5] Tesar and Barker,[6] Vejrazka *et al.*,[7] Geers *et al.*,[8] Hadžiabdić and Hanjalić,[9] and El Hassan *et al.*,[10] among many others.

These and other studies have already established that a circular jet impinging upon a flat-surface perpendicularly can be divided into three distinct regions, which comprise of a free-jet region, a stagnation region, and a wall-jet region. These regions result from the fact that, after the free jet impinges upon the flat-surface, it essentially turns perpendicularly and moves radially away from the stagnation point along the flat-surface. Past investigations have revealed that the exact flow behaviour is sensitive towards the jet Reynolds number, shear layer characteristics,

[a] Author to whom correspondence should be addressed. Electronic mail: dthnew@ntu.edu.sg

turbulence level, jet exit to surface separation distance, and possible presence of flow excitations. Nevertheless, the basic flow behaviour surrounding circular jet-flat surface impingements is relatively well-known—certainly more so than other impinging jet configurations. Along this line of thought then, it is worthwhile to note that circular jet impingements upon surfaces that deviate away from flat geometries received significantly lesser attention. In particular, the global flow dynamics associated with the use of curved surfaces remain comparatively less well understood.

One of the earliest in-depth studies focusing on the vortex structures and flow behaviour of circular jet impingements upon curved surfaces was performed by Cornaro *et al.*[11] They made use of cylinder-to-jet diameter-ratios of approximately D/d = 2.6–5.6, Reynolds numbers of 6000–20 000, and separation distances of 1–4 jet diameters. Their qualitative smoke wire visualization study revealed that convex surface jet impingement behaviour differs significantly from that associated with a flat-surface and is highly sensitive towards the separation distance and relative curvature. For instance, the stagnation point was observed to suffer strong radial oscillations, though this issue could be mitigated by reducing the separation distance. Additionally, transitions to turbulence were also delayed when the jet-to-curvature diameter ratio was increased. To quantify the findings made by Cornaro *et al.*,[11] Fleischer *et al.*[12] extracted key vortical locations which showed that larger jet-to-curvature diameter ratios allowed the jet vortices to remain attached to the convex surface longer and break up later. Reducing the separation distance, on the other hand, led to earlier vortex-separations and break-ups. However, due to their impinging jet configurations, these key vortical locations along the convex surfaces tend to occur within a relatively small angular range of approximately 19°–54° away from the impingement point across all test cases reported. As such, it will be interesting to see if other impinging jet configurations can achieve a wider range of key vortical locations and ascertain the impact of the flow scenario parameters better.

It should be clear from these earlier studies that convex surface jet impingement is a highly complex and intricate flow configuration. More comprehensive mean flow field characteristics for a Re = 25 000 circular jet impinging upon a D/d = 4 convex cylinder at a separation distance of four jet-diameters were provided by Esirgemez *et al.*[13] through the use of laser Doppler anemometry technique. Their extensive results demonstrated that the circular free jet would become highly three-dimensional after it impinged upon and wrapped around the convex cylinder. Unfortunately, little detailed information on the latter flow mechanism was provided. In addition, they observed that the presence of a convex cylinder did not alter the circular jet flow characteristics significantly until approximately 0.05 jet diameter away from the impingement point on the convex cylinder. As mean flow results were only reported in this study, it remains unknown whether Esirgemez *et al.*[13] observed any oscillations of the stagnation point. More recently, Singh *et al.*[14] conducted a joint experimental and numerical investigation on jet-cylinder impingements but with significantly larger diameter-ratios of approximately D/d = 4–8.4. While they placed a heavy emphasis on heat transfer characteristics, it is interesting to note from some of their numerical results that a recirculating region will be formed at the cylinder lee-side due to the jet impingement. In particular, it is observed that the recirculating region size is sensitive towards the separation distance (i.e., which ranged from 4 to 16 jet diameters for the study), which indicates that the recirculating region size is dependent upon the key vortical locations occurring along the convex cylindrical surface. Interestingly, the flow patterns of the recirculating region also suggested that flow spirals away from the region towards the cylinder ends.

The present study was motivated by a desire to shed more light upon the global flow dynamics of jet impingement on convex surfaces by utilizing circular cylinders as the impingement surfaces of choice. First, while smoke visualization results provided by Cornaro *et al.*[11] and Fleischer *et al.*[12] had given us first-hand appreciations of the associated flow fields and quantitative information on the vortex-separation and break-up locations, they were very much limited in terms of temporal flow evolutions and by their very qualitative nature. There is a need to further resolve the temporal and spatial aspects of the flow dynamics quantitatively to reveal further details. Second, it is difficult to infer the underlying flow dynamics from the mean flow field characteristics presented by Esirgemez *et al.*[13] and Singh *et al.*,[14] even though they did provide valuable information on the time-averaged effects conferred by the unsteady flow phenomenon. Finally and perhaps more importantly, jet-cylinder impingement studies thus so far have not come up with a topological plausible

flow model to corroborate observations made in earlier investigations. With these in mind, it will be timely to take a closer look at this flow configuration to understand how the free-jet vortex structures and their dynamics evolve as they impinge upon and convect along convex cylindrical surfaces.

To accomplish this, a laser-induced fluorescence (LIF) based flow visualization and digital particle-image velocimetry (DPIV) study was conducted on a low Reynolds number circular jet impinging upon circular cylinders of various diameters at a separation distance where jet ring-vortices are highly coherent and stable. The purpose is to track the vortex structures right from they are formed along the jet shear layers after the jets exhaust from the nozzle, all the way to their impingements upon the cylindrical surfaces and their subsequent flow interactions. Special attention will be paid towards the developments of the vortex structures after the impinging jet re-orientates itself along the cylindrical surfaces and the resulting key vortical locations. From the results, flow interpretations will be constructed and compared against well-established jet-flat surface impingement flow dynamics. Finally, effects of cylinder-to-jet diameter ratio upon the flow dynamics and wall shear stress distributions and magnitudes will also be assessed as part of the overall understanding.

II. EXPERIMENTAL SETUP AND PROCEDURES

A. Experimental apparatus

The experiments were performed in a recirculating jet-testing water tank setup shown schematically in Fig. 1, where the internal dimensions of the water tank measured 400 mm (W) × 400 mm (H) × 800 mm (L). It was constructed out of 15 mm thick clear Plexiglas sheets, which offered good optical access from multiple viewpoints. A centrifugal pump took water from a small reservoir and channelled it through an electromagnetic flowmeter, a needle valve, and a jet apparatus, before the water was exhausted into the quiescent water tank via a circular nozzle. Flow-conditioning devices such as a diffuser, honeycombs, fine screens, and a 25:1 ratio contraction chamber were incorporated into the jet apparatus to straighten the flow and improve its initial turbulence levels. The freely exhausting jet from the circular nozzle would impinge upon a circular test cylinder and any excess water would overflow back into the small reservoir via polyvinyl chloride (PVC) pipes located at the back wall of the water tank. It is worthwhile to point out that very similar setups have been used by New and Tsovolos[15] and Shi and New[16] on other jet flow studies previously.

The diameter and length of the circular nozzle were d = 20 mm and L = 40 mm, respectively, and with a mean jet velocity of U = 0.11 m/s, the jet Reynolds number was estimated to be approximately Re = 2200. No flow forcing was used in the present study and the initial jet exit conditions are shown in Fig. 2. Three different circular acrylic cylinders of D/d = 1, 2, and 4 were used and they were located at a jet-to-surface separation distance of H/d = 4 throughout. No attempts were made to look into the effects of separation distance variations in the present investigation, as the focus was on the impingement behaviour of coherent and well-developed large-scale

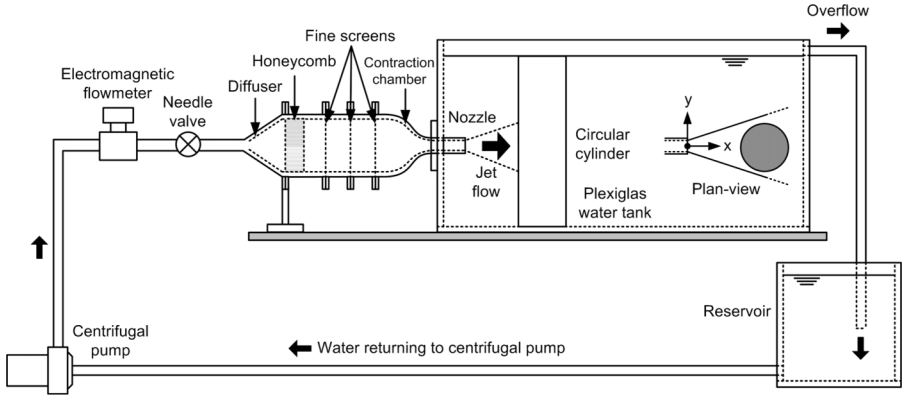

FIG. 1. Schematics of the recirculating jet-impingement setup.

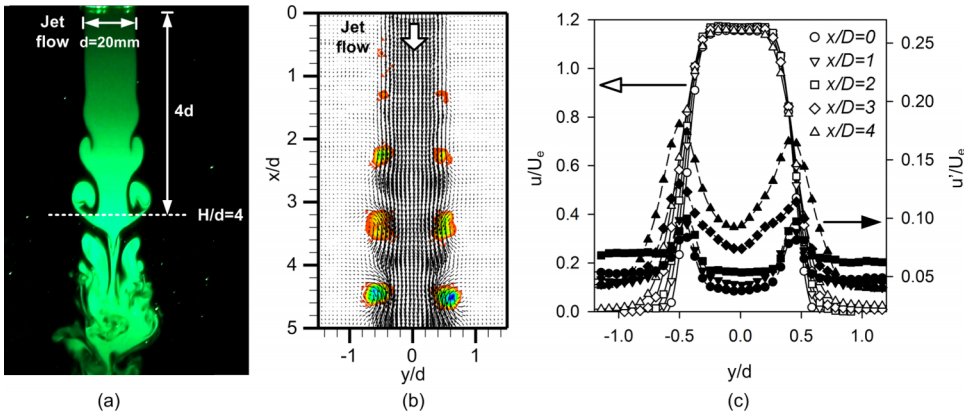

FIG. 2. Initial flow conditions of the free jet as depicted through (a) streamwise LIF visualization, (b) λ_2 criterion vortex-core detection, and (c) mean jet exit velocity and turbulence intensity distributions. Empty and solid symbols associated with mean velocity and turbulence intensity data-points, respectively. Similar-shaped symbols represent data-points at the same downstream locations.

jet ring-vortices. It should be mentioned that separation distances of H/d = 2, 4, and 6 had been tested and H/d = 4 configuration was found to have more developed and coherent jet ring-vortices impinging upon the cylinders, as can be inferred in Fig. 2(a). H/d = 2 and 6 configurations, on the other hand, led to jet ring-vortices which were either not fully developed or more incoherent by the time they reached the cylinders. The test cylinder surfaces were entirely covered with thin black adhesive paper to avoid significant light reflections caused by the laser sheet illuminations during the LIF and DPIV experiments. Depending on the required visualization/measurement plane, the cylinders were arranged either vertically or horizontally. Finally, while Fig. 2(c) shows slight asymmetries in the turbulence intensity profiles for x/D = 3 and 4 locations, note that they can be attributed to naturally occurring wave instabilities and rolling-up of the jet shear layer at these locations shown in Fig. 2(a). However, they do not confer appreciable distortions to the overall symmetry of the subsequent jet-impingement flow fields as shown by the flow visualization and measurements' results presented later. This is also supported by Cornaro *et al.*,[11,17] where similar minor turbulence intensity asymmetries observed in their initial free jet flows did not affect the symmetries of their flow fields appreciably as well.

B. LIF visualizations

For LIF experiments, fluorescein disodium fluorescent salt was dissolved and released into the jet fluid prior to its entry into the jet apparatus. Laser beam from a 1 W, 532 nm wavelength, LaVision continuous-wave diode-pumped solid state laser was split into two separate beams using a beam splitter-plate, before they were used to form two thin laser sheets via sheet-forming optics. These two laser sheets entered the water tank from both sides at the same height and illuminated the impinging jets along the nozzle centreline. Using two laser sheets instead of one would reduce the effects of shadows casted by the cylinders and allow better visualizations of the flow fields. Due to the excitation of the fluorescent dye by the laser, the jet fluid would show up as green colour during the LIF experiments, while ambient fluid would appear as black. A remotely controlled digital single-lens reflex camera with a 50 mm, f1.4 lens located above the water tank was then used to record videos of the LIF visualizations in 1920 px × 1080 px resolution at 25 frames-per-second for subsequent analysis.

C. DPVI measurements

As for the DPIV experiments, a Dantec Dynamics 2D system comprising of an Evergreen 200 mJ double-pulsed Nd:YAG laser, four-megapixel FlowSense CCD camera, synchronization, and frame-grabber cards was used. As will be seen later, flow visualization results demonstrate that

the flow fields are highly symmetrical about the flow symmetry plane, and hence, measurements were conducted for only half of the symmetric flow fields to maximize the available laser power during the DPIV experiments. Scattered light from the 20 μm sized, 1.03 g/cm^3 polyamide seeding particles dispersed in both the jet fluid and water in the tank was captured by the 2×1 binned CCD camera, which output particle images at 2048 px $\times$ 1024 px resolution in double-frame mode. The experiments were performed at 14 Hz without any particular preference to the exact flow phase, which was sufficiently fast to track the jet-impingement behaviour well. Control of the DPIV experiments, and transfer and post-processing of the particle images were performed using Dantec DynamicStudio™ software.

A two-step multi-grid cross-correlation scheme with initial and final interrogation window sizes of 128px $\times$ 128px and 32px $\times$ 32px, respectively, was used to determine the raw velocity vectors. Based on the cross-correlation procedures, the particle-images were interrogated with a sub-pixel accuracy of approximately 0.1 pixel. These vectors were subsequently subjected to peak, range, and moving-average validations to remove any spurious vectors before their substitute vectors were calculated from a 3-point by 3-point neighbour scheme to reach the final velocity vector maps that were used to derive other flow quantities. DPIV measurement resolution is approximately 0.27 of the initial jet shear layer thickness and thus able to resolve the jet ring-vortex structures adequately. Finally, DPIV measurements have been performed according to the guidelines put forward by Keane and Adrian,[18] in which the uncertainty level of the velocity vectors was estimated to stay within ±1% of the actual velocity components. Based on the experimental setup and flow conditions, the overall experimental uncertainty in the velocity measurements was estimated to be approximately ±2.4%, according to the principles described in Moffat.[19]

III. RESULTS AND DISCUSSIONS

Figure 3 shows instantaneous LIF flow visualization snapshots captured for jet-impingements upon flat-surface and D/d = 4, 2, and 1 cylinders for a first-hand appreciation of the resulting flow behaviour. For ease and consistency in the description of the vortical behaviour, nomenclatures relatively similar to those used in Fleischer *et al.*[12] will be adopted here. For instance, vortex initiation refers to when vortex ring-vortices are formed along the jet shear layer, while vortex-dipole formation refers to the formation of a mushroom-shaped vortex structure formed by a pair of opposite-signed ring-vortex and wall separated vortex along the impingement surface. Vortex separation refers to when a vortex-dipole detaches from the surface, while vortex-coalescence is when the vortex-dipoles interact in proximity and coalesce. Finally, vortex-breakup is when the coalesced vortices become increasingly more incoherent and eventually transit into flow turbulence due to viscous effects.

For flat-surface jet impingement at the present separation distance, ring-vortex initiation distance prior to their impingement upon the surface is located at approximately 3-3.5d downstream

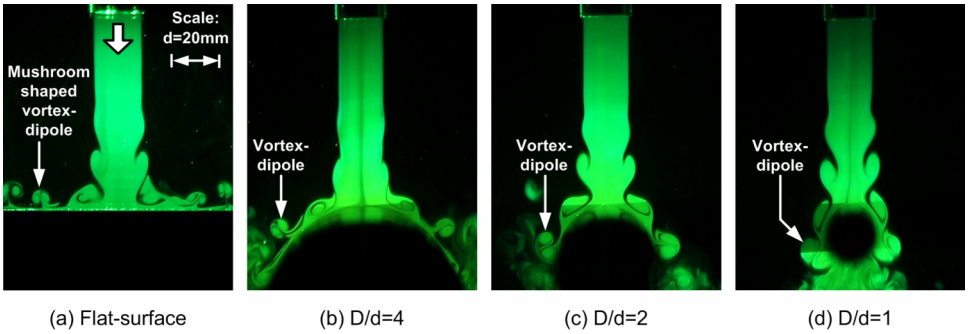

FIG. 3. Instantaneous LIF flow images for jet-impingement upon (a) flat-surface, (b) D/d = 4, (c) D/d = 2, and (d) D/d = 1 cylinders, demonstrating the dependence of the vortex-dipole formation locations on the impingement surface geometry.

from the nozzle exit. As the large-scale ring-vortex impinges upon the flat surface, it moves radially away from the stagnation point and outwards along the wall. At the same time, its core size reduces significantly due to vortex-stretching (caused by the expanding ring diameter) and the wall boundary layer is induced to separate at approximately 1.5-2d away from the stagnation point. Jet ring-vortex and the wall separated vortex subsequently combined to produce a mushroom-shaped vortex-dipole which separates from the flat surface later. These observations are in good agreement with the flow visualization results obtained by Popiel and Trass[4] and Cornaro *et al.*[11] While such scalar dye-based visualizations are usually adequate in the near-field regions, a λ_2 criterion was applied on the DPIV velocity field measurements to validate our qualitative observations. This criterion has been successfully proposed and demonstrated by Jeong and Hussain[20] to detect vortex cores successfully even in high flow shears and hence used here to highlight the vortex core developments during the jet impingement process. The results are presented in Fig. 4, where highlighted regions in the time-sequenced DPIV results with λ_2 criterion identified vortex cores signify the behaviour of the vortex cores. Note that the first DPIV result is set arbitrarily to t = 0 s and selected such that it approximately shows the jet ring-vortex immediately after it impinges upon the cylindrical surface. It can be seen that the formation of and subsequent interactions between the jet ring-vortex (i.e., A) and wall separated vortex (i.e., S_1) are consistent with observations made in Fig. 3(a).

As for D/d = 4 cylinder jet impingement shown in Fig. 3(b), similar to flat-surface impingement seen previously, the wall boundary layer will separate shortly after the jet ring-vortices impinge upon the cylindrical surface, producing mushroom-shaped vortex-dipoles that detach from the cylindrical surface. Despite the curved cylindrical surface, the gross flow behaviour resembles quite closely to what was observed for flat-surface impingement earlier. However, this is not too surprising as this particular cylinder has the largest diameter among all three test cylinders here and thus deviates the least from the flat-surface configuration. When the cylinder diameter-ratio decreases to D/d = 2 and 1, Figs. 3(c) and 3(d) indicate qualitatively that the impinging jet flow will continue to wrap itself around the cylinder and following the contour of the cylindrical surface, with corresponding delays in the wall boundary layer separation and vortex-dipole formation locations. Considering that the exact flow blockage presented by each cylinder is directly proportional to its diameter-ratio, these preceding observations appear to be consistent. On the other hand, it is difficult to identify the exact vortex-dipole formation and separation locations reliably from the flow visualization results.

To address this, time-sequenced DPIV results will be presented and used to identify some of these key vortical locations. Their availability here not only allows better quantitative assessment of the changes to the key vortical locations but also enables a better appreciation of the overall flow dynamics. Before these results are presented, however, an example time-sequenced LIF flow image associated with the D/d = 4 cylinder test case is shown in Fig. 5, where flow developments of both the jet ring-vortex and wall separated vortex cores (i.e., A and S_1, respectively) can be observed. Note that these LIF flow images are selected such that they correspond closely to the

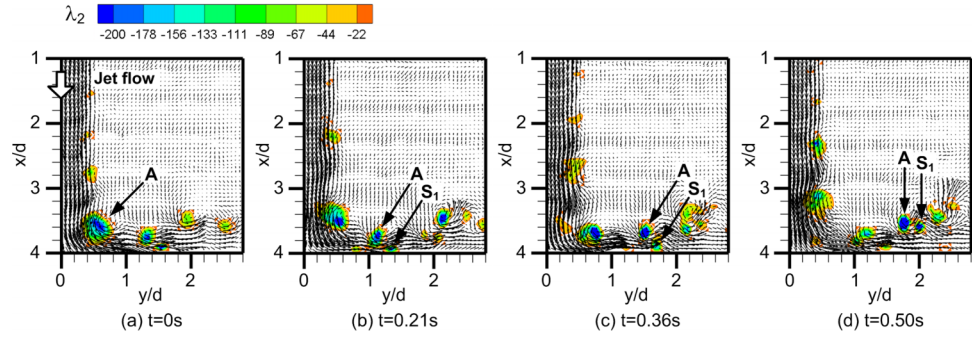

FIG. 4. Instantaneous DPIV velocity fields and λ_2 criterion identified vortex behaviour associated with flat-surface jet impingement.

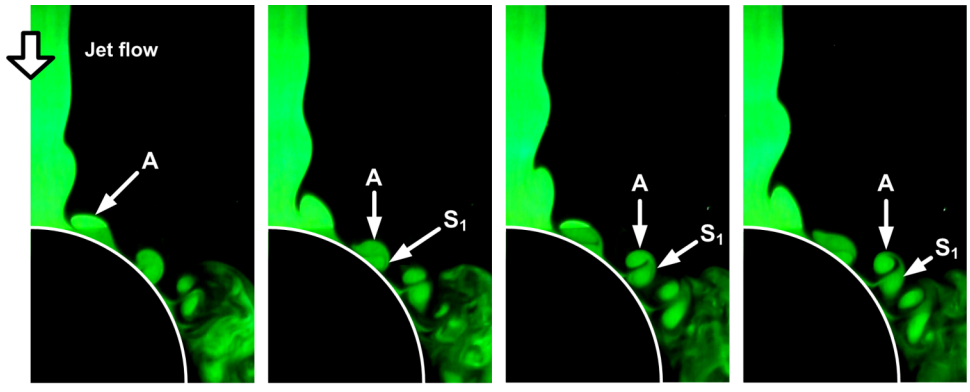

FIG. 5. Time-sequenced LIF flow images depicting the behaviour of the jet ring-vortex and wall separated vortex cores during the jet impingement process for D/d = 4 cylinder.

time-sequenced DPIV results associated with the same test cylinder presented in Fig. 6, such that readers can better relate the qualitative vortical changes to the quantitative DPIV measurements of the key vortical locations.

Figure 6 shows three different sets of time-sequenced instantaneous velocity vector fields and λ_2 criterion identified vortex behaviour for the D/d = 4 cylinder test case, based on different minimum λ_2 cut-off values of −100, −200, and −400. This is to assess the uncertainty of using three different minimum λ_2 cut-off values in the identification of the key vortex cores associated with jet-cylinder impingement. Similar to Fig. 4 presented earlier, the first DPIV result in each set is arbitrarily set to t = 0 s and selected such that it approximately shows the jet ring-vortex immediately after it impinges upon the cylindrical surface. Key vortical locations can be isolated by examining the instantaneous changes to vortex core behaviour as identified through the λ_2 criterion. For instance, vortex-dipole formation locations are defined as those whereby wall separated vortex-cores are first observed to initiate adjacent to the jet ring-vortex cores for all test cylinders. Similarly, vortex-dipole separation locations are defined as those whereby their vortex-cores are observed to detach from the cylindrical surface, which are further confirmed by the underlying velocity vector distributions. While the DPIV measurement frequency is limited to only 14 Hz (i.e. 0.071 s interval between consecutive DPIV velocity fields), the low velocities of the impinging jets mean that the key flow behaviour and vortex structures can still be tracked satisfactorily to ascertain the key vortical locations reliably.

Furthermore, note that a maximum λ_2 cut-off value of −22 is used here throughout to remove the background λ_2 value. Since it only serves to remove the background to better isolate the various vortex-core regions, this maximum cut-off value does not materially impact upon the vortex-core region identification and is used regardless of the exact minimum λ_2 cut-off value. From the very small angular discrepancies in the identified vortex-dipole formation and vortex-separation locations across all three different minimum λ_2 cut-off values, Fig. 6 demonstrates that the exact minimum λ_2 cut-off values used here do not materially impact upon the determination of the vortex-dipole formation and vortex-separation locations, provided the minimum λ_2 cut-off value is not too small to highlight the vortex-core regions properly. Using an intermediate minimum λ_2 cut-off value of −200, the figure shows that vortex-dipole formation occurs at approximately 43.6° from the flow symmetry plane as shown in Fig. 6(b-ii), while vortex-separation occurs further downstream at about 51.1° as seen in Fig. 6(b-iii). Thereafter, the vortex-dipole continues to convect almost tangentially away from the vortex-separation point at approximately 70° from the flow symmetry plane. As a matter of consistency, λ_2 criterion identified vortex behaviour for the two other test cylinders based on a similar minimum λ_2 cut-off value will now be presented in Fig. 7.

For the smaller D/d = 2 cylinder shown in Fig. 7(a), the qualitative jet impingement behaviour as seen from the top is relatively similar to the D/d = 4 cylinder in terms of the key vortical flow

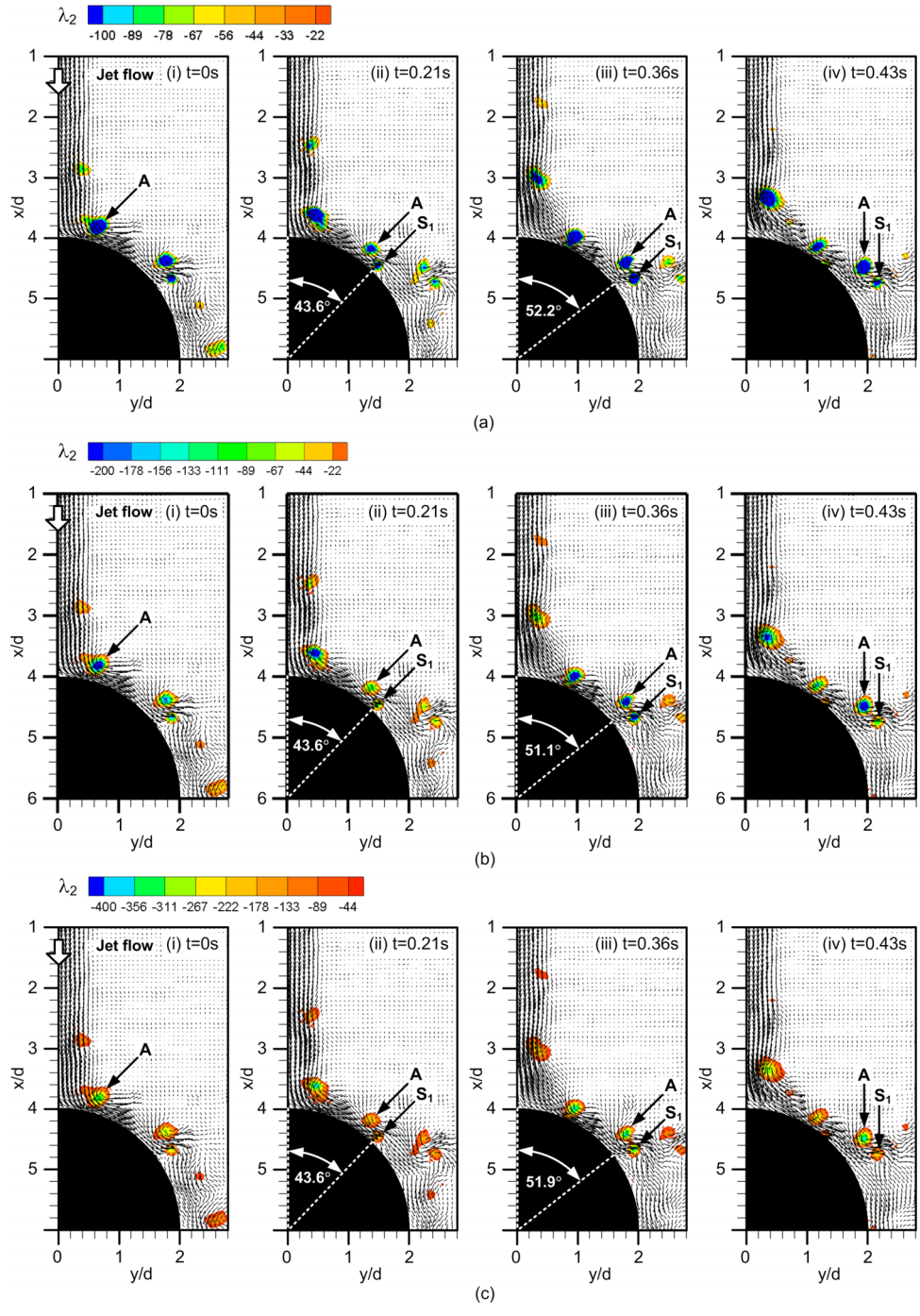

FIG. 6. Comparison of instantaneous DPIV velocity fields and λ_2 criterion identified vortex behaviour associated with jet impingement upon D/d = 4 cylinder as taken from the top-view, based on different minimum λ_2 criterion values of (a) −100, (b) −200, and (c) −400.

changes. Nevertheless, the figure indicates that the jet flow remains attached to the cylindrical surface for a comparatively longer distance, with vortex-dipole formation and vortex-separation occurring significantly further downstream. For a better comparison, vortex-dipole formation and vortex-separation locations are determined from the vortical motions presented in Figs. 7(a-ii) and 7(a-iii). In this case, they are estimated to be approximately 86° and 99.6° respectively, and validated the flow visualization results. Additionally, the trajectory of the vortex-dipoles separated from

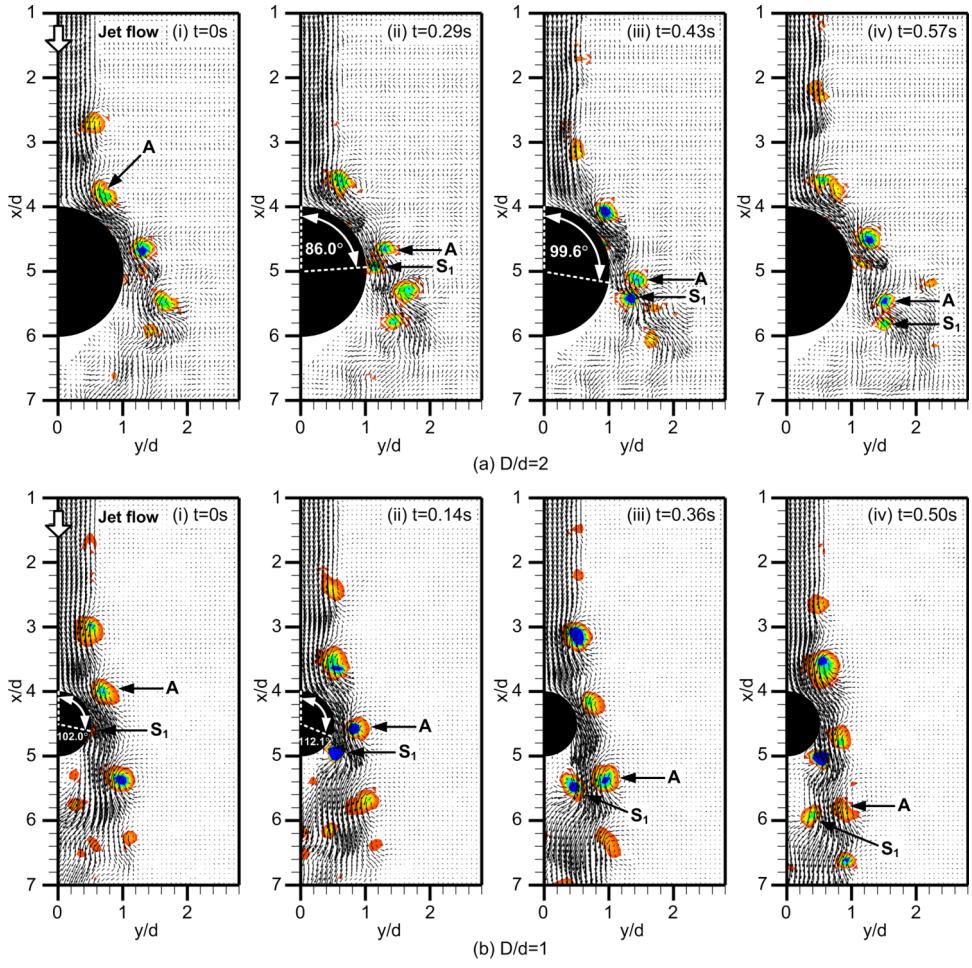

FIG. 7. Instantaneous DPIV velocity fields and λ_2 criterion identified vortex behaviour associated with jet impingement upon (a) D/d = 2 and (b) D/d = 1 cylinders, as taken from the top-view.

the cylindrical surface occurs at a smaller angle of approximately 20° from the flow symmetry plane as well. In fact, this trend continues when the cylinder diameter is further reduced to D/d = 1, as shown in Figs. 3(d) and 7(b). In this case, the vortex-dipole forms at an even further downstream location of about 102° and the vortex-separation location occurs at approximately 112.1° as shown in Figs. 7(b-i) and 7(b-ii). Interestingly, the separated vortex-dipoles convect further downstream in a relatively streamwise direction with little veering away from the flow symmetry plane. It should be highlighted that the vortex-dipoles may occasionally convect towards the lee-side of the cylinder and closer towards the flow symmetry plane.

At this point, it will be interesting to track and compare the overall trajectories of the jet ring-vortex and wall separated vortex core locations, from the point where the former is first observed along the jet shear layer to when the separated vortex-dipole has convected significantly away from the test cylinder. Therefore, vortex-core trajectories associated with all three test cylinders are shown in Fig. 8. For the sake of consistency, these vortex-core trajectories were extracted from the same flow sequences from which λ_2 results are determined and presented in Figs. 6 and 7 earlier. The only difference is that the vortex-core trajectories were extracted from λ_2-identified vortex-core locations for the entire flow sequence, rather than at selected intervals. From Fig. 8, it can be observed that the vortex-dipoles generally convect away from the cylindrical surface tangentially after they separate from the latter, regardless of the exact cylinder diameter-ratio. Interestingly though, those associated with the D/d = 4 cylinder exhibit a tendency to rotate anticlockwise upon

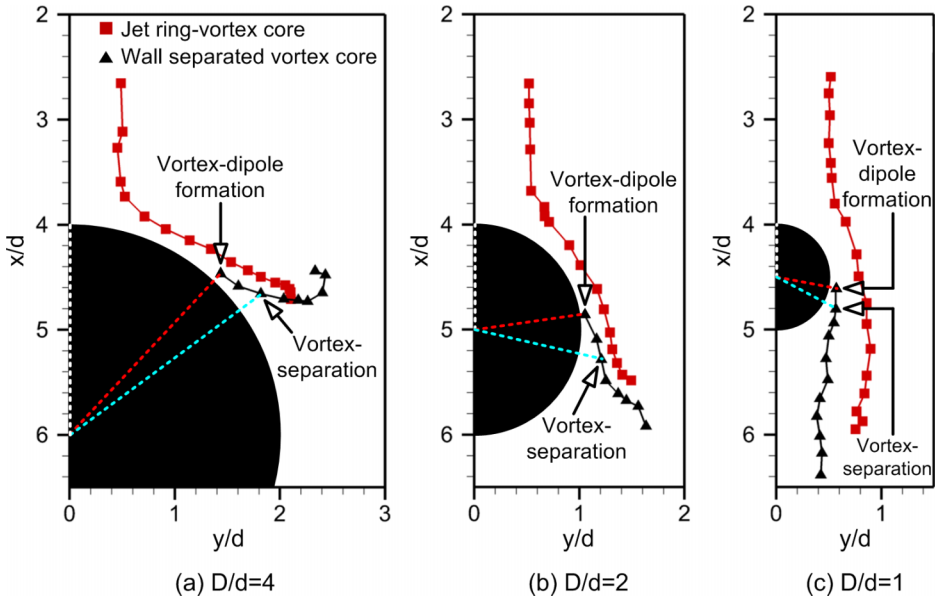

FIG. 8. Primary and secondary vortex-core trajectories associated with jet impingement upon (a) $D/d = 4$, (b) $D/d = 2$, and (c) $D/d = 1$ cylinders, as taken from the top-view.

themselves eventually, due to the wall-separated vortex moving upstream when the vortex-dipole is at some significant distance away from the cylindrical surface. Corroborating the results shown in Figs. 6–8, it is found that vortex-separations typically occur between a relatively narrow angular range of approximately 10°–15° downstream of the vortex-dipole formation locations, at least for the present study. Finally, it is worthwhile to note that as the cylinder diameter-ratio reduces, the trajectories of the jet ring-vortex and wall separated vortex core that make up the vortex-dipole tend to diverge more.

Note that the use of λ_2 criterion on the DPIV results proves to be useful here, as the rapid dissipation of scalar fluorescent dye due to the convection of the separated vortex-pairs makes it difficult to accurately assess their subsequent trajectories. In fact, as the cylinder diameter becomes gradually smaller, vortex-breakup phenomenon becomes progressively more rapid. These preceding evidences support earlier findings reported by Cornaro *et al.*[11] and Fleischer *et al.*[12] and quantitatively confirm that the jet flow will separate later from the cylindrical surface if the cylinder diameter is smaller. Note that even though time-sequenced λ_2 criterion identified vortex behaviour is used to estimate the preceding vortex-dipole formation and vortex-separation locations, the discrepancies in these locations between different test cylinders are sufficiently different to confirm tangible influences conferred by the changes in cylinder diameter-ratio. Furthermore, time-sequenced λ_2 criterion identified vortex behaviour shown in Figs. 6 and 7 has the additional benefit of depicting the overall dynamics of the various vortex structures, much similar to time-sequenced flow visualizations. In particular, the use of DPIV measurements to track the vortical behaviour here means that the key vortex locations can be isolated more accurately. It is also worthwhile to point out that the jet ring-vortex core size is more significantly reduced after jet impingement for a larger diameter cylinder, indicative of accentuated vortex-stretching and that the ring-vortices "wrap" themselves around the cylindrical surfaces. The "wrapping around" is only partial, however, due to the wake formations immediately aft of the cylinders. Other than that, the general vortical behaviour is generally consistent across all the test cylinders studied here.

Figure 9 shows the vortex structures and behaviour associated with the impingement process for the $D/d = 4$, 2, and 1 cylinders but captured from the side-view and thus along the cylinder straight-edge. Note that the vortical motion and behaviour are remarkably similar for the three cylinders, regardless of their exact diameter. The flow similarity extends to the wall boundary layer separation, vortex-dipole formation and vortex-separation locations, and the DPIV results,

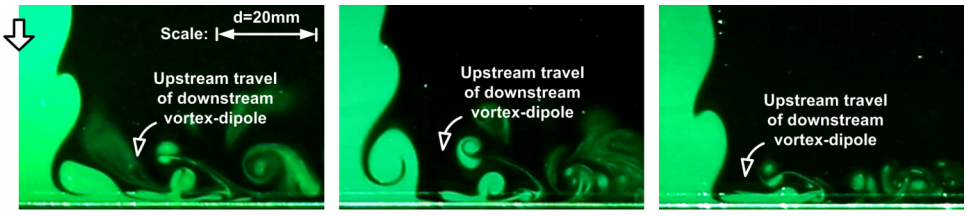

FIG. 9. Instantaneous LIF flow images taken from the side-view for jet-impingement upon (a) D/d = 4, (b) D/d = 2, and (c) D/d = 1 cylinders.

where they do not vary significantly between the three test cylinders. Hence, the following flow description and discussion will be applicable for all three cylinders. Unlike the case for flat-surface jet impingement, the ring-vortex core size does not remain relatively invariant regardless of the viewing orientation. In this case, the ring-vortex core size is drastically reduced shortly after it impinges upon, turn and convect along the wall radially. This is in contrast to the flow images seen from the top-view presented in Fig. 3, where the ring-vortex core size reduction is significantly more moderate. The sudden reduction in the ring-vortex core size may again be attributed to the vortex-stretching effects imparted to the ring-vortex segment along the cylinder straight-edge, as the ring-vortex segment wraps itself along the cylindrical surface while continue to convect downstream.

Despite the sharp reduction in the ring-vortex core size, Fig. 9 shows that the smaller ring-vortex continues to induce wall boundary layer to separate to form a smaller mushroom-shaped vortex-dipole that subsequently lifts off and separates from the cylindrical surface. Intriguingly, the separated vortex-dipole does not simply convect along the cylinder straight-edge, as would be the case for flat-surface jet impingements. Instead, it moves upstream, "leapfrogs" over, and interacts with another vortex-dipole, which has just been formed. During the entire interaction process, the ring-vortex core size continues to be reduced, though it remains relatively coherent. The preceding flow visualizations are supported by the DPIV results presented in Fig. 10, where a representative sequence of flow events for D/d = 4 cylinder is shown. Note that the corresponding DPIV results for the other two test cylinders are not presented here due to their similarities and for the sake of brevity. Other than the presence of significant vortex-stretching, such a curious flow behaviour is also likely to be a result of the not insignificant induced velocities caused by the close proximity of multiple vortex-dipoles. This will be elaborated later when interpretations of the 3D flow dynamics are presented. Results indicate that the vortex-dipole forms at approximately x/d = 1.3 location, while vortex-separation occurs at a short distance thereafter at approximately x/d = 1.5 location. These locations are comparatively closer to the impingement point than that seen for flat-surface jet impingement earlier, thus providing quantitative evidence of the effects due to non-uniform vortex-stretching rates upon the ring-vortices.

With the availability of DPIV velocity field results, mean skin friction coefficient distributions along both the convex cylindrical surfaces and cylinder straight-edges can be determined. To obtain these results, wall shear stresses along both the convex cylindrical surfaces and cylinder straight-edges were determined, based on the normal velocity gradients along the surfaces, as

$$\tau_w = \mu \left. \frac{\partial u}{\partial y} \right|_w .$$

For flat-surface and cylinder straight-edges, these velocity gradients can be extracted from the Cartesian-coordinate based mean velocity fields in a relatively straight forward manner. First, wall locations in the velocity fields were identified as the empty vector points along the expected flat-surface and cylinder straight-edge boundaries. Subsequently, velocity information adjacent to the wall was then used to determine the velocity gradient, assuming a constant wall normal height Δy throughout based on the finest grid resolution of the measured velocity fields. The procedures used for the convex cylindrical surfaces were relatively similar, except that the coordinate system

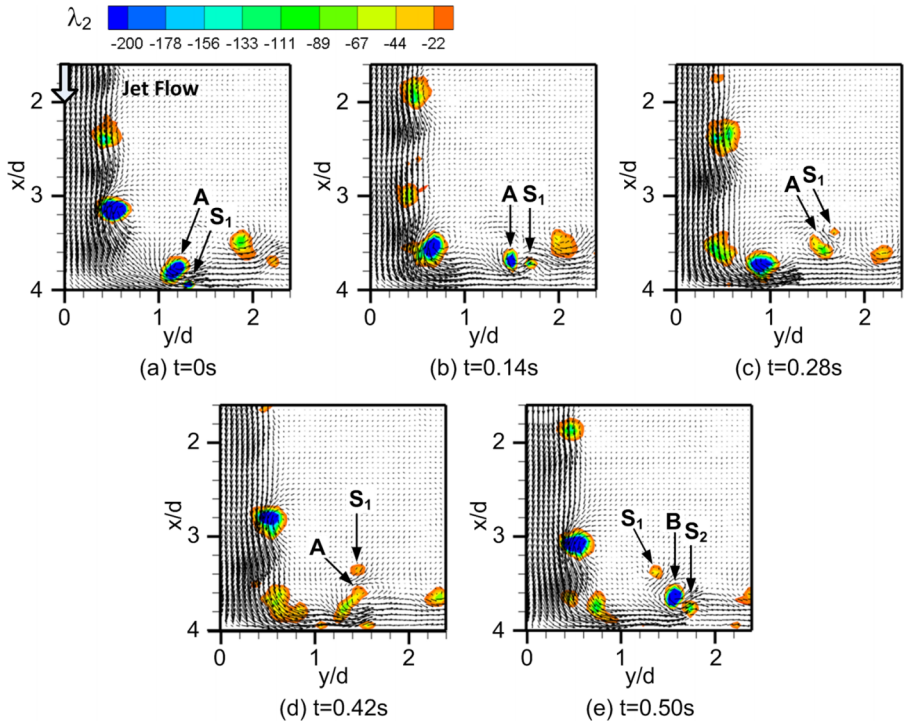

FIG. 10. Instantaneous DPIV velocity fields and λ_2 criterion identified vortex behaviour associated with jet impingement upon D/d = 4 cylinder, as taken from the side-view.

for the velocity fields had to be converted from a Cartesian to polar coordinate system to obtain the wall-normal velocity gradients. In this case, the wall shear stresses were calculated by invoking

$$\tau_{r\vartheta} = \mu\left[r\frac{\partial}{\partial r}\left(\frac{v_\vartheta}{r}\right) + \frac{1}{r}\frac{\partial v_r}{\partial \vartheta}\right].$$

Once the wall shear stress distributions had been determined, they were non-dimensionalized to obtain the skin friction coefficient as

$$C_f = \frac{\tau_w}{\frac{1}{2}\rho U^2}$$

and their comparisons are presented in Fig. 11. Note that results for the flat-surface jet impingement test case are included in both plots to allow better comparisons here.

For flat-surface jet impingement skin friction coefficient result shown in the figure, its trend is in good agreement with El Hassan *et al.*,[10] where they made use of both DPIV and electrochemical techniques to determine the mean skin friction coefficients. For the present flat-surface jet impingement, the skin friction coefficient increases in a relatively linear manner from the impingement point (i.e., y/d = 0) until it reaches a maximum level at approximately y/d = 0.8 location. This location is upstream of the wall boundary layer separation location (i.e., approximately 1.5-2d as observed from experiments and discussed earlier) and prior to the formation of the wall separated vortex, as observed in Fig. 4 earlier. It decreases gradually thereafter before levelling off towards an asymptotic value at the measurement window limit of the current DPIV experiments (i.e., y/d ≈ 5). Similar trends are also observed for jet impingements upon the cylinder straight-edges, as shown in Fig. 11(a). Furthermore, maximum skin friction coefficient location occurs closer to the impingement point as the diameter-ratio decreases, which agrees well with what was observed in Fig. 10 earlier. On the other hand, the skin friction coefficient distributions are far more intriguing along the convex cylindrical surfaces, as can be discerned from Fig. 11(b). While the trends are grossly similar and that maximum skin friction coefficient levels are comparable to those along the cylinder

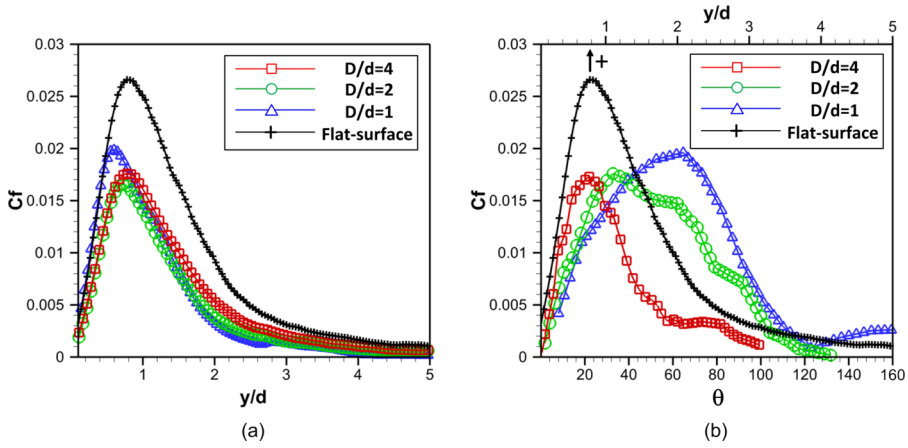

FIG. 11. Comparisons of mean skin friction coefficients along the (a) cylinder straight-edges and (b) convex cylindrical surfaces for all three test-cylinders, as estimated from DPIV velocity measurements. Results for flat-surface jet impingement are also included in each plot for comparisons.

straight-edges depicted in Fig. 11(a), it is clear that the locations at which they occur are increasingly further along the cylindrical surface as the cylinder diameter-ratio reduces. For instance, these locations are estimated to be approximately $\theta = 24°$, 34°, and 66° for $D/d = 4$, 2, and 1 test cylinders, respectively. It is worthwhile to point out that these locations occur well before the wall boundary layer separates to form the vortex-dipole subsequently. Hence, this downstream shift in the location as the cylinder diameter-ratio decreases correlates well with similar delays in the vortex-dipole formation and vortex-separation locations directly observed from the DPIV results earlier.

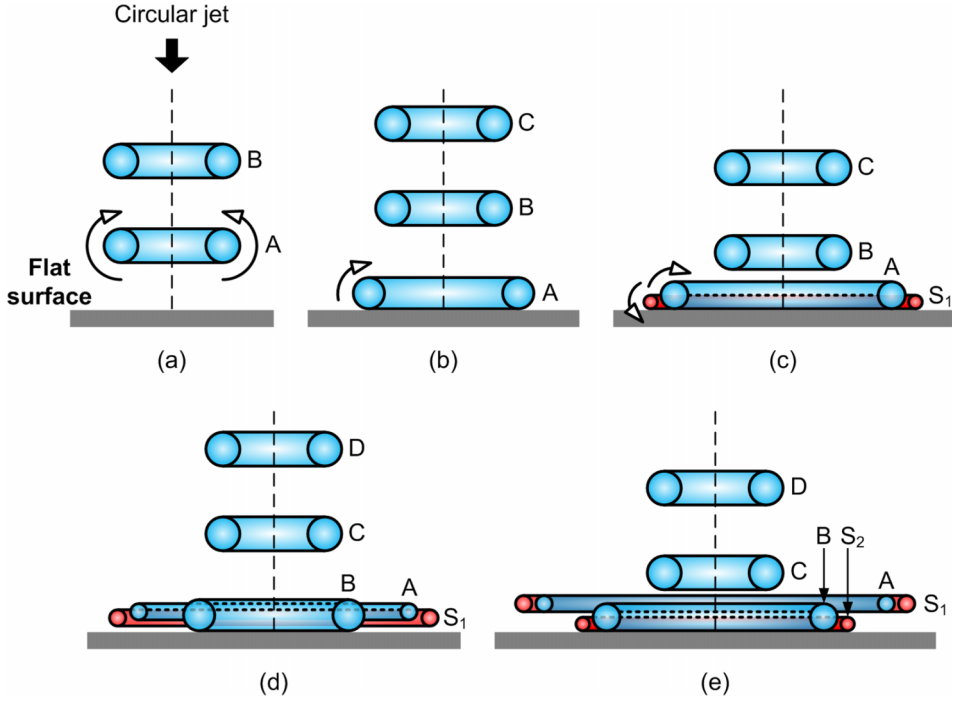

FIG. 12. Flow dynamics interpreted for jet impingement upon a flat-surface. Vortex filaments are depicted in partial cross-sections.

Furthermore, regardless of whether they are taken along the cylindrical surfaces or cylinder straight-edges, the maximum skin friction coefficients are reduced by approximately 26%-35% as compared to the flat-surface configuration, depending on the exact test cylinder. Collating with the results presented earlier, it would appear that significantly more gradual changes in the jet flow directions made possible by the use of round cylinders instead of a flat-surface produces remarkable reductions in the wall shear stresses. Rather than subjecting the jet to a 90° change in its flow direction for flat-surface jet impingement, the use of round cylinders reduces this drastic change in the jet flow direction by offering comparatively smaller flow blockages. Note that flow blockage is 100% for flat-surface jet impingements.

The preceding results provide us with a good opportunity to examine and clarify their overall flow dynamics, particularly in terms of corroborating the vortex behaviours along both the cylindrical surface and cylinder straight-edge. Before the flow interpretations for jet impingement upon round cylinders are presented, Fig. 12 first shows the classical flow dynamics associated with jet impingement upon a flat-surface. In the figure, jet ring-vortices and wall separated vortices are depicted in blue and red, respectively, as well as shown in their cross-sectional forms for simplification. True to the results shown in Figs. 3(a) and 4 (and those associated with earlier studies),

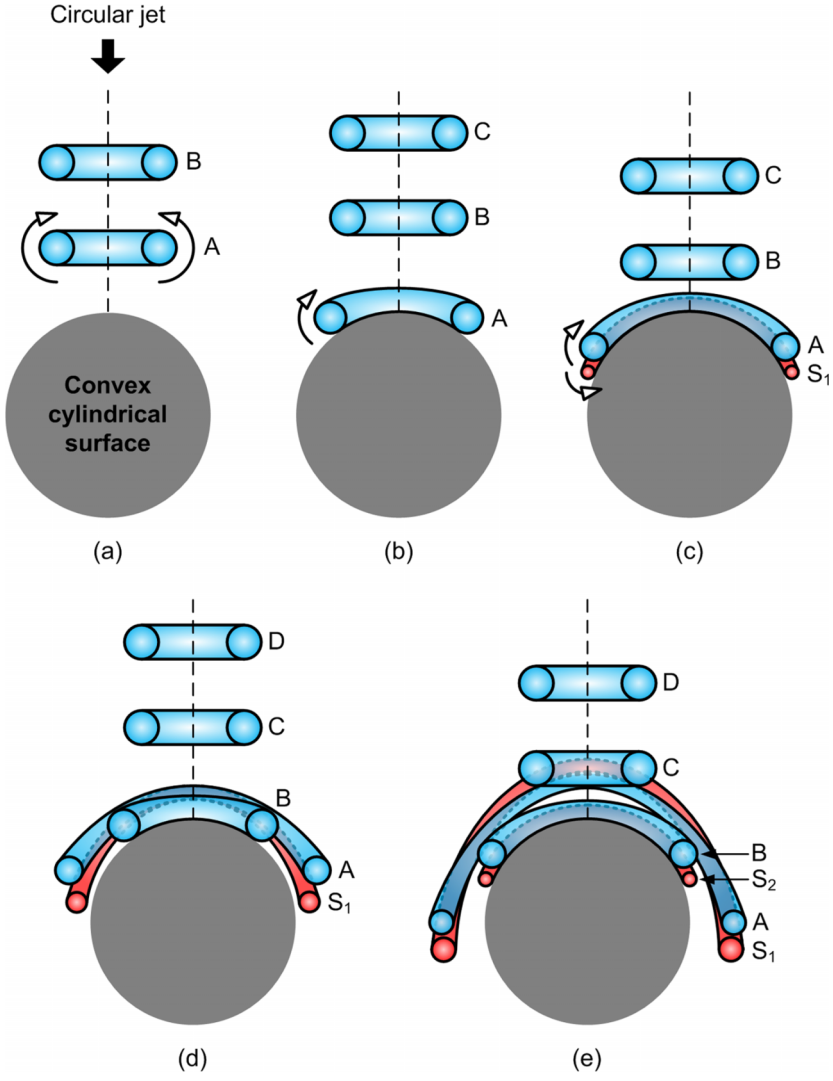

FIG. 13. Interpretations of the flow dynamics associated with jet-cylinder impingement behaviour as observed from the top-view. Vortex filaments are depicted in partial cross-sections.

the figure illustrates a flow situation whereby the diameter of the jet ring-vortex expands after it impinges upon the flat-surface. As its diameter increases when it moves away from the jet impingement point, it induces the wall boundary layer to separate and produce a secondary vortex of opposite rotational sense, together which they form a vortex-dipole that separates from the flat-surface later.

On the other hand, Fig. 13 shows the generalized flow developments put forward for jet ring-vortices impinging upon a typical convex cylinder with diameter $D/d \geq 1$, as seen from the top-view. As the ring-vortex A collides with the convex cylindrical surface, streamwise jet momentum ensues that it begins to initiate the process of wrapping itself around the convex cylindrical surface, as depicted in Figs. 13(a) and 13(b). As a result, segments of ring-vortex A stretch themselves as they convect along the convex cylindrical surface, shown in Fig. 13(c). During this time, stretching of the ring-vortex A along this plane is expected to initiate and accentuate gradually. At this point, interactions between the primary ring-vortex A and the boundary layer along the convex surface lead to the separation of the latter and result in a secondary ring-vortex S_1 that possesses an opposite rotational sense. This would agree well with the flow behaviour observed in Figs. 3(b)–3(d) earlier. Due to the wrapping of ring-vortex A around the cylindrical surface, the outline of the secondary ring-vortex S_1 takes on a relatively similar distorted form, as depicted in Fig. 13(c). Subsequently, close proximity between ring-vortices A and S_1 results in their pairing to form a vortex-dipole seen in the flow visualization images earlier. As the next ring-vortex

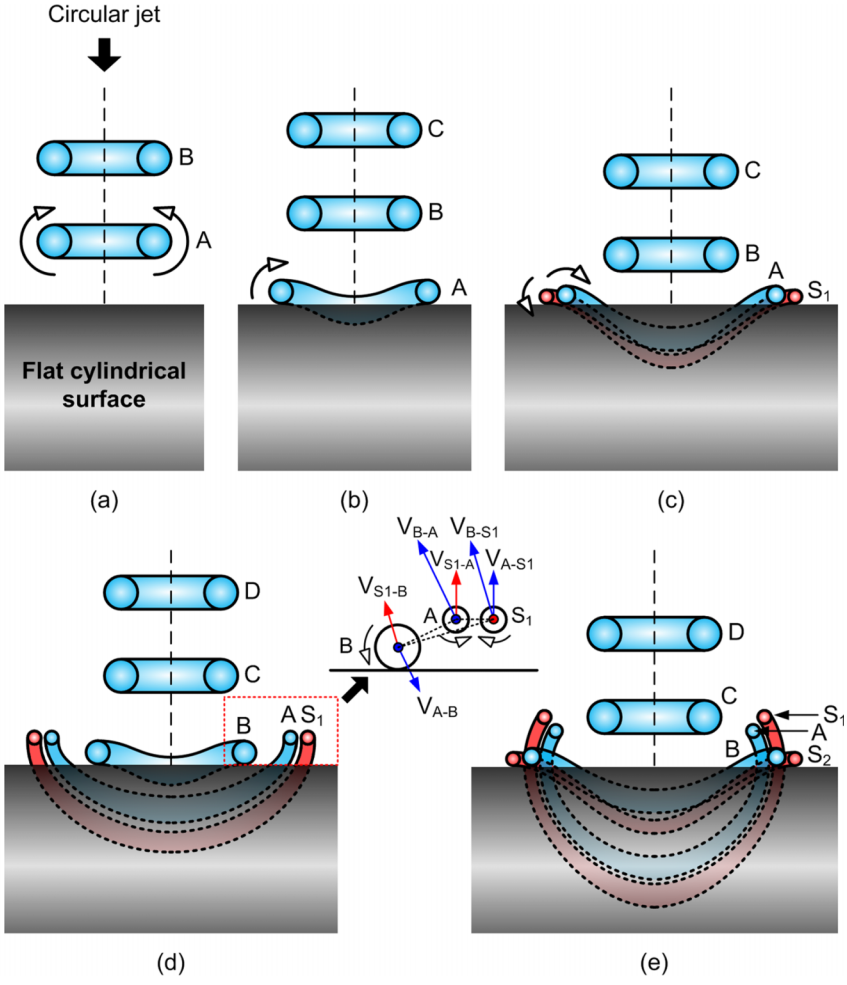

FIG. 14. Interpretations of the flow dynamics associated with jet-cylinder impingement behaviour as observed from the side. Vortex filaments are depicted in partial cross-sections.

B impinges upon the cylindrical surface, it undergoes similar flow dynamics to produce another secondary ring-vortex S_2 and the flow cycle repeats.

Along the cylinder straight-edge, however, as shown in Fig. 14, the flow dynamics are quite different. In contrast to Fig. 13, ring-vortex A does not wrap itself around the cylinder. Nevertheless, ring-vortex A is influenced by vortex-stretching and its vortex-core size diminishes after it impinges upon the straight-edge, as shown in Fig. 14(a). Note that in this case though, as depicted in Fig. 14(b), the vortex-stretching results from the ring-vortex A moving away from the impingement point along this plane, as well as the its movement along the cylindrical surface. Subsequently, Figs. 14(c) and 14(d) show that ring-vortex A induces the wall boundary layer to separate and produce a secondary ring-vortex S_1, which then interacts to produce a vortex-dipole. Induced velocities due to each vortex core of the vortex-dipole [V_{A-S1} and V_{S1-A} in Fig. 14(d)] will produce a net velocity moving away from the cylinder straight-edge. Thus, the vortex-pair will eventually separate from the straight-edge under the influence of this net velocity. Up to this point, much of the flow behaviour remains similar to that of a jet impinging upon a flat-surface as described in Fig. 12.

However, as the flow progresses, strong interactions between the vortex-dipole and the upstream ring-vortex B will result in significant mutually induced velocities. Due to the rotation of ring-vortex B, velocities towards the upstream direction are induced in both vortex cores A and S_1. As shown in the close-up view in Fig. 14(d), ring-vortex B will induce velocity components V_{B-A} and V_{B-S1} upon the vortex-dipole such that it will move towards the general upstream direction. As a result, this vortex- dipole subsequently moves upstream and "leapfrog" the vortex-dipole produced by ring-vortices B and S_2 a moment later, as depicted in Fig. 14(e), before interacting with vortices B and S_2 eventually and dissipate through viscous effects. This intriguing flow difference is conjectured to result from a combination of vortex-stretching and centrifugal effects as the ring-vortices wrap themselves around the cylinders, which are not present in flat-surface jet impingements. Due to flow acceleration of ring-vortices A and S_1 segments along the cylindrical surface as they move away from the impingement point initially, it is reasonable to put forward the argument that these two effects act together to produce conditions more favourable towards interactions between multiple vortex-dipoles along the cylinder straight-edge.

IV. CONCLUSIONS

Detailed flow dynamics associated with a laminar jet impinging upon a convex cylinder with cylinder-to-jet diameter-ratios, ranging from 1, 2, and 4, and at a jet-to-cylinder separation distance of four jet diameters, have been documented in the present paper. In particular, LIF and DPIV results taken along both the cylindrical surfaces and cylinder straight-edges are correlated to provide a detail look into how the jet ring-vortices behave after their impingements. After impingement, jet ring-vortices induce wall boundary layer to separate and together, they form mushroom-shaped vortex-dipoles which later separate from the cylindrical surfaces. Vortex-dipole formation and separation locations are delayed further along the cylindrical surface when the cylinder diameter reduces. Trajectory of the vortex-pairs is also observed to increasingly deviate away from the original jet streamwise direction when the diameter-ratio increases. While relatively similar flow behaviour reminiscence of jet-flat surface impingements is observed along the cylindrical straight-edge up to the point when the ring-vortices and wall separated vortices form vortex-dipoles, subtle but intriguing flow differences are observed thereafter. In particular, the vortex-dipoles gradually turn and move towards the upstream direction and interact with another vortex-dipole that has just been formed, instead of convecting downstream steadily as initially expected.

Wall shear stress results corroborate well with the instantaneous DPIV results and that maximum wall shear stress levels for jet impingements upon cylindrical surface and straight-edges are significantly lower than that associated with flat-surface jet impingements. The overall flow dynamics observed in the present study are encapsulated in three-dimensional flow interpretations to address outstanding questions in earlier investigations, in terms of reconciling the jet-impingement behaviour along the cylindrical surface and straight-edge of the round cylinder in a consistent manner. It also puts forward plausible explanations to account for the intriguing upstream vortical motions

and interactions experienced by the vortex-dipoles along the cylinder straight-edges. In this case, significant mutually induced velocities between the various vortex structures due to vortex-stretching effects caused by the ring-vortices wrapping themselves around the convex cylindrical surfaces, as well as close proximity between the ring-vortices and vortex-dipoles, are found to be able to account for the present observations.

ACKNOWLEDGMENTS

The authors gratefully acknowledge the support for the present study by a Nanyang Technological University Start-Up Grant. The second author gratefully acknowledges the support for the present study by a Nanyang Technological University Ph.D. Research Scholarship.

[1] C. D. Donaldson and R. S. Snedeker, "A study of free jet impingement. Part 1. Mean properties of free and impinging jets," J. Fluid Mech. **45**(2), 281–319 (1971).
[2] N. Didden and C. M. Ho, "Unsteady separation in a boundary layer produced by an impinging jet," J. Fluid Mech. **160**, 235–256 (1985).
[3] C. C. Landreth and R. J. Adrian, "Impingement of a low Reynolds number turbulent circular jet onto a flat plate at normal incidence," Exp. Fluids **9**(1-2), 74–84 (1990).
[4] C. O. Popiel and O. Trass, "Visualization of a free and impinging round jet," Exp. Therm. Fluid Sci. **4**(3), 253–264 (1991).
[5] M. Fairweather and G. Hargrave, "Experimental investigation of an axisymmetric, impinging turbulent jet. 1. Velocity field," Exp. Fluids **33**(3), 464–471 (2002).
[6] V. Tesař and J. Barker, "Dominant vortices in impinging jet flows," J. Visualization **5**(2), 121–128 (2002).
[7] J. Vejrazka, J. Tihon, P. Marty, and V. Sobolik, "Effect of an external excitation on the flow structure in a circular impinging jet," Phys. Fluids **17**(10), 105102 (2005).
[8] L. F. G. Geers, M. J. Tummers, and K. Hanjalić, "Particle imaging velocimetry-based identification of coherent structures in normally impinging multiple jets," Phys. Fluids **17**(5), 055105 (2005).
[9] M. Hadžiabdić and K. Hanjalić, "Vortical structures and heat transfer in a round impinging jet," J. Fluid Mech. **596**, 221–260 (2008).
[10] M. El Hassan, H. H. Assoum, V. Sobolik, J. Vétel, K. Abed-Meraim, A. Garon, and A. Sakout, "Experimental investigation of the wall shear stress and the vortex dynamics in a circular impinging jet," Exp. Fluids **52**(6), 1475–1489 (2012).
[11] C. Cornaro, A. S. Fleischer, and R. J. Goldstein, "Flow visualization of a round jet impinging on cylindrical surfaces," Exp. Therm. Fluid Sci. **20**(2), 66–78 (1999).
[12] A. S. Fleischer, K. Kramer, and R. J. Goldstein, "Dynamics of the vortex structure of a jet impinging on a convex surface," Exp. Therm. Fluid Sci. **24**(3), 169–175 (2001).
[13] E. Esirgemez, J. W. Newby, C. Nott, S. M. Ölçmen, and V. Ötügen, "Experimental study of a round jet impinging on a convex cylinder," Meas. Sci. Technol. **18**(7), 1800 (2007).
[14] D. Singh, B. Premachandran, and S. Kohli, "Experimental and numerical investigation of jet impingement cooling of a circular cylinder," Int. J. Heat Mass Transfer **60**, 672–688 (2013).
[15] T. H. New and D. Tsovolos, "Influence of nozzle sharpness on the flow fields of V-notched nozzle jets," Phys. Fluids **21**, 084107 (2009).
[16] S. Shi and T. H. New, "Some observations in the vortex-turning behaviour of noncircular inclined jets," Exp. Fluids **54**, 1614 (2013).
[17] C. Cornaro, A. S. Fleischer, M. Rounds, and R. J. Goldstein, "Jet impingement cooling of a convex semi-cylindrical surface," Int. J. Therm. Sci. **40**, 890–898 (2001).
[18] R. D. Keane and R. J. Adrian, "Theory of cross-correlation analysis of PIV images," Appl. Sci. Res. **49**, 191–215 (1992).
[19] R. J. Moffat, "Describing the uncertainties in experimental results," Exp. Therm. Fluid Sci. **1**, 3–17 (1988).
[20] J. Jeong and F. Hussain, "On the identification of a vortex," J. Fluid Mech. **285**, 69–94 (1995).